2001

Analysis of the Effect of Porous Wall Interference on Transonic Airfoil Flutter

Castro, B.M.; Jones, K.D.; Ekaterinaris, J.A.; Platzer, M.F.

Castro, B.M., Jones, K.D., Ekaterinaris, J.A. and Platzer, M.F., "Analysis of the Effect of Porous Wall Interference on Transonic Airfoil Flutter," AIAA Paper No. 2001-2725, Anaheim, California, June 2001.
https://hdl.handle.net/10945/37199

AIAA−2001−2725

ANALYSIS OF THE EFFECT OF POROUS WALL INTERFERENCE ON TRANSONIC AIRFOIL FLUTTER

B.M.Castro, K.D.Jones, J.A.Ekaterinaris and M.F.Platzer
Naval Postgraduate School
Monterey, CA

31st AIAA Fluid Dynamics Conference & Exhibit
11−14 June 2001 / Anaheim, CA

Analysis of the Effect of Porous Wall Interference on Transonic Airfoil Flutter

B. M. Castro,[*] K. D. Jones,[**] J. A. Ekaterinaris,[†] and M. F. Platzer[‡]

Naval Postgraduate School
Monterey, California

Abstract

A numerical investigation of the influence of the wind tunnel walls on the transonic, two-degree-of-freedom, bending/torsion, flutter characteristics of the NLR7301 section is carried out in the time domain. A parallelized, implicit, time-accurate, two-dimensional, compressible, thin-layer Navier-Stokes flow-solver is coupled with a two-degree-of-freedom structural model. A three-block deforming grid is used for the discretization of the domain including the airfoil and wind tunnel walls. Two types of porous-wall boundary-conditions are implemented and tested for the boundaries representing the tunnel walls. The first applies a porous, inviscid boundary condition and the second applies a porous, viscous one. The type of porous boundary condition is found to significantly influence both steady and unsteady solutions. Computed pressure distribution for steady, transonic flow show better agreement with the experimental results when a viscous, porous boundary condition is applied at the wind tunnel walls. Results show that the free-flight flutter behavior may differ significantly from the behavior found in a porous wind tunnel because of the strong dependence on the tunnel porosity parameter and the proximity of the walls.

Nomenclature

a_∞ = free-stream speed of sound
c = chord length
C_L = lift coefficient
C_m = pitching moment coefficient
C_p = pressure coefficient
D_h = plunge-damping coefficient
D_α = pitch-damping coefficient
f = frequency in Hertz
h = plunge displacement (positive downward)
$\hat{h}$ = maximum half amplitude of plunge
I_α = moment of inertia about x_p
k = reduced frequency, $\omega c/U_\infty$
k_α = reduced natural pitching frequency, $\omega_\alpha c/U_\infty$
k_h = reduced natural plunging frequency, $\omega_h c/U_\infty$
K_h = spring constant for plunging
K_α = spring constant for pitching
L = lift
m = mass of the wing
M = pitching moment
$\mathbf{M}_\infty$ = free-stream Mach number
Pr = Prandtl number
Re = Reynolds number
S_α = static moment, $x_\alpha m$
t = time
U_∞ = free-stream speed
u, w = Cartesian velocity components
x = coordinate along chord
x_p = leading edge to elastic axis distance
x_α = elastic axis to center of mass distance
$\dot{x}|_{wall}$ = velocity component of airfoil surface
$\dot{y}|_{wall}$ = velocity component of airfoil surface
y^+ = dimensionless normal wall distance
α = angle of incidence
$\bar{\alpha}$ = average angle of incidence
$\hat{\alpha}$ = maximum half amplitude of α
α_0 = spring-neutral angle of attack
δ_h = non-dim. plunge-damping coef., $D_h/(2\sqrt{mK_h})$
δ_α = non-dim. pitch-damping coef., $D_\alpha/(2\sqrt{I_\alpha K_\alpha})$
ω = circular frequency, $\omega = 2\pi f$
ω_h = undamped natural bending freq., $\sqrt{K_h/m}$
ω_α = undamped natural torsional freq., $\sqrt{K_\alpha/I_\alpha}$
Φ = phase angle between pitch and plunge
σ = porosity parameter, Eq. (16)
τ = dimensionless time, ta_∞/c
$(\dot{})$ = differentiation with respect to t
$(\,)'$ = differentiation with respect to τ
$(\,)_c$ = corrected value
$(\,)_i$ = initial value
$|_{wall}$ = quantity on the surface of the airfoil
$(\,)_\infty$ = free-stream value

---

[*] Graduate Student, Student Member, AIAA

[**] Research Assistant Professor, Senior Member, AIAA

[†] Senior Research Scientist, NEAR Inc., Associate Fellow, AIAA

[‡] Professor, Fellow, AIAA

I. Introduction

Historically, great efforts have been devoted to experimental and theoretical investigations of the transonic flutter characteristics of airfoils, because the transonic dip associated with the flutter speed of typical aircraft wings poses a serious problem for flight safety. In the study carried out by Weber et al.,[1] comparisons of an unbounded flow calculation with experimental results obtained by means of a wind tunnel test suggested significant wall interference effects. It was found by Castro et al.[2] that the inclusion of the wind tunnel walls in the formulation of the problem can significantly improve the agreement of numerical and experimental results for steady as well as unsteady computations.

This study is a continuation of the work presented in Ref. 2, where it was found that both the porosity and the way of applying the corresponding boundary condition influenced the results of both steady and unsteady computations for the NLR7301 airfoil inside a wind tunnel at transonic speeds. In that work, modeling the porosity of the tunnel wall required a very careful construction of the grid where the cells were approximately equally spaced at the wall regions. This was necessary because some grid cells were treated as solid walls while others were treated as holes in order to achieve the desired porosity. For example, a 50% porosity was modeled by treating four consecutive grid cells as holes, the next four as solid walls, and so on. The drawback of this approach was that a very limited number of possible values of porosity could be simulated due to the finite number of grid cells at the wind tunnel walls. In fact, only porosity values of 25%, 50%, and 75% were feasible. Furthermore, the plenum chamber pressure was not included in the model.

A primary goal of the present investigation was to improve the porous wind-tunnel wall model used in the previous study, specifically, providing solution uniqueness and including the plenum pressure. As previously mentioned, the previous model provided a number of ways to achieve the same porosity, each resulting in a different solution. Furthermore, the requirement for equally spaced gridding along the tunnel walls should be eliminated. In the present investigation, the approach presented by Mokry et al.[3] is used. The normal velocity at the porous wall is proportional to the pressure difference between the plenum chamber and the test section at the wall. This model allows a much more continuous variation of flow parameters and does not require an equally spaced grid along the walls.

Time-accurate flutter computations require large computing times until limit-cycle is reached. Computational efficiency can be improved by taking advantage of parallel architectures. The computational domain is divided into three blocks to enable discretization of the full geometry, including the wind tunnel test section. This makes the approach suitable for parallel computation. Therefore, a newly developed parallel version of the code uses three Pentium II 400 MHz PC's to carry out the computations, assigning one block to each processor. The boundary conditions are transferred from one machine to another via a specific library called Message Passing Interface (MPI). The cluster of Linux PC's are effective in performing the parallel computations and also in reducing the wall-clock time.

The flow solver and the aeroelastic models used in the present investigation have been tested and validated extensively in previous studies for a variety of flow conditions. For example, the flow solver and the turbulence models have been tested for subsonic flow[4,5,6] and for transonic flow.[7] The aeroelastic model has been implemented and tested in Ref. 8 for inviscid flow calculations and in Ref. 1 for viscous, transonic flow.

The transition modeling capability of the code was demonstrated in Refs. 1 and 4. Nevertheless, because previous results of Ref. 1 showed that transition only slightly improved the numerical results, transition modeling was not used in the present investigation, assuming fully turbulent flow.

The ability of the multi-block version of the flow solver to accurately predict the flow over a stationary airfoil in a wind tunnel by including porous wall effects was demonstrated in the previous work.[2] Comparisons with experimental results obtained in the DLR-Göttingen wind tunnel[9,10] have demonstrated that inclusion of wind-tunnel effects is the key to obtaining both steady-state pressure distribution and flutter characteristics in better agreement with the experiment.

In this paper, the effect of tunnel wall interference on transonic flutter/limit-cycle prediction is investigated in further detail. To this end, parametric studies of porosity, tunnel height, and Mach number are conducted. Numerical solutions are obtained for an airfoil free to oscillate in two-degrees-of-freedom in transonic flow and the results are compared with the measurements of Knipfer et al.[9]

II. Aerodynamics

The aeroelastic behavior of an airfoil can be predicted by solving the aerodynamic flow in combination with the structural dynamic response. The aerodynamic equations are presented first and the method

used to compute the structural response is presented in the next section.

A. Governing Equations

The time-dependent, compressible, thin-layer, two-dimensional Navier-Stokes equations in the strong conservation-law form and curvilinear coordinate system (ξ, ζ) are:

$$\partial_t \hat{\mathbf{Q}} + \partial_\xi \hat{\mathbf{F}} + \partial_\zeta \hat{\mathbf{G}} = Re^{-1} \partial_\zeta \hat{\mathbf{S}} \tag{1}$$

where $\hat{\mathbf{Q}}$ is the vector of conservative variables,

$$\hat{\mathbf{Q}} = \frac{1}{J} \begin{Bmatrix} \rho \\ \rho u \\ \rho w \\ e \end{Bmatrix}, \tag{2}$$

$\hat{\mathbf{F}}$ and $\hat{\mathbf{G}}$ are the inviscid flux vectors,

$$\hat{\mathbf{F}} = \frac{1}{J} \begin{Bmatrix} \rho U \\ \rho u U + \xi_x p \\ \rho w U + \xi_z p \\ (e+p)U - \xi_t p \end{Bmatrix}, \tag{3}$$

$$\hat{\mathbf{G}} = \frac{1}{J} \begin{Bmatrix} \rho W \\ \rho u W + \zeta_x p \\ \rho w W + \zeta_z p \\ (e+p)W - \zeta_t p \end{Bmatrix}, \tag{4}$$

and $\hat{\mathbf{S}}$ is the thin-layer approximation of the viscous fluxes in the ζ direction (normal to the airfoil surface),

$$\hat{\mathbf{S}} = \frac{1}{J} \begin{Bmatrix} 0 \\ \mu m_1 u_\zeta + (\mu/3) m_2 \zeta_x \\ \mu m_1 w_\zeta + (\mu/3) m_2 \zeta_z \\ \mu m_1 m_3 + (\mu/3) m_2 m_4 \end{Bmatrix}, \tag{5}$$

where

$$m_1 = \zeta_x^2 + \zeta_z^2, \tag{6}$$
$$m_2 = \zeta_x u_\zeta + \zeta_z w_\zeta, \tag{7}$$
$$m_3 = \partial_\zeta (u^2 + w^2)/2 + (\gamma - 1)^{-1} Pr^{-1} \partial_\zeta (a^2), \tag{8}$$
$$m_4 = \zeta_x u + \zeta_z w. \tag{9}$$

The terms U and W are the contravariant velocity components given by:

$$U = u\xi_x + w\xi_z + \xi_t \tag{10}$$
$$W = u\zeta_x + w\zeta_z + \zeta_t \tag{11}$$

and J is the metric Jacobian, where

$$J^{-1} = x_\xi z_\zeta - x_\zeta z_\xi \ . \tag{12}$$

The pressure is related to the other variables through the equation of state for an ideal gas

$$p = (\gamma - 1)\Big[e - \rho(u^2 + w^2)/2\Big] \ . \tag{13}$$

Eqs. (1-13) are nondimensionalized using c as the reference length, a_∞ as the reference speed, c/a_∞ as the reference time, ρ_∞ as the reference density and $\rho_\infty a_\infty^2$ as the reference energy.

B. Numerical Method

The algorithm for the numerical solution of these equations was developed and tested in Ref. 5. Oscillatory motion of the airfoil in the wind tunnel implies use of deforming grids. Therefore, modifications of the numerical algorithm according to the suggestions of Ref. 11 were incorporated in order to enable solutions of the governing equations for flow problems that require temporal grid-deformation. The implicit, deforming-grid, time-marching algorithm is given by:

$$\begin{aligned} &\Big[I + h_\xi \Big(\nabla_\xi \hat{A}^+_{i,k} + \Delta_\xi \hat{A}^-_{i,k}\Big)^p\Big] \\ &\times \Big[I + h_\zeta \Big(\nabla_\zeta \hat{B}^+_{i,k} + \Delta_\zeta \hat{B}^-_{i,k} - Re^{-1}\delta_\zeta \hat{M}_{i,k}\Big)^p\Big] \\ &\times \Big(\hat{Q}^{p+1}_{i,k} - \hat{Q}^p_{i,k}\Big) \\ = \ &-\Big[\Big(\hat{Q}^p_{i,k} - \hat{Q}^n_{i,k}\Big) \\ &+ h_\xi \Big(\hat{F}^p_{i+1/2,k} - \hat{F}^p_{i-1/2,k}\Big) \\ &+ h_\zeta \Big(\hat{G}^p_{i,k+1/2} - \hat{G}^p_{i,k-1/2}\Big) \\ &- Re^{-1} h_\zeta \Big(\hat{S}^p_{i,k+1/2} - \hat{S}^p_{i,k-1/2}\Big)\Big] \ . \end{aligned} \tag{14}$$

In Eq. (14), $h_\xi = \Delta\tau/\Delta\xi$ etc., $\hat{A}^\pm = \partial\hat{F}/\partial\hat{Q}$ etc. are the flux Jacobian matrices and ∇, Δ and δ are the forward, backward and central difference operators, respectively. The quantities $\hat{F}_{i+1/2,k}$, $\hat{G}_{i,k+1/2}$ and $\hat{S}_{i,k+1/2}$ are numerical fluxes. The superscript $(\cdot)^n$ denotes the physical time step, and the superscript $(\cdot)^p$ refers to Newton sub-iterations within each physical time step.

The inviscid fluxes, $\hat{F}$ and $\hat{G}$, are evaluated by means of the Osher's third-order accurate, upwind-biased scheme.[12,13] Linearization of the left-hand side of Eq. (14) is performed by evaluating the flux Jacobian matrices, A and B, with the Steger-Warming flux-vector splitting.[14] The viscous fluxes are computed with second-order central differences. Furthermore, a

standard minmod TVD flux limiter[12] is used to eliminate numerical oscillations at shocks developed at transonic Mach numbers.

Time accuracy is improved by performing Newton sub-iterations to convergence within each physical step. These sub-iterations minimize the linearization and factorization errors and help drive the left-hand side of Eq. (14) to zero.

The turbulence modeling is based either on the standard algebraic model of Baldwin and Lomax[15] (BL) or one equation models of Baldwin and Barth[16] (BB) or Spalart and Allmaras[17] (SA). The eddy-viscosity obtained from the models is used for the computation of the fully turbulent region. The present simulations were performed with the SA model.

C. Three Block Grid

Modeling of the wind tunnel geometry requires a mesh which is very long in the streamwise direction, compared to its height. Accurate computation of the boundary layer is most easily performed on a C-grid. However, construction of a single block, C-grid would require a very skewed grid and an excessive number of grid points in regions far from the airfoil. Furthermore, it would not be possible to maintain grid orthogonality close to the walls using a single block grid. These problems can be minimized by using a three block grid, shown schematically in Fig. 1, where the governing equations are solved in each block, separately.

The first block (1) is a C-type grid and contains the airfoil and the wind tunnel walls above and below it. The grid spacing in the normal direction close to the grid boundaries representing the tunnel walls in block (1) is appropriate only for inviscid computations. The second and third grid blocks are Cartesian-type inviscid grids and model the upstream and downstream portions of the wind tunnel, respectively. These blocks have a narrow but finite region of overlapping with the first grid block. Data transfer between the blocks is obtained by linear interpolation of the conservative variables (ρ,ρu,ρw,e).

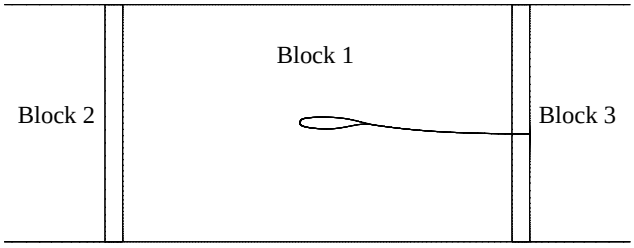

Fig. 1. Schematic of the three block grid.

D. Boundary Conditions

For inviscid flow solutions, the viscous terms on the RHS of Eq. (1) are set to zero, and flow-tangency boundary conditions are used at the surface of the airfoil. For Navier-Stokes solutions, the no-slip condition is applied. Density and pressure are extrapolated to the surface for both Euler and Navier-Stokes solutions.

For unsteady motions, the flow-tangency and no-slip conditions are modified to include the local motion of the airfoil which also contributes to the pressure on the surface. Therefore, the momentum equation normal to the surface (ζ direction) is solved to predict the pressure for a viscous flow more accurately

$$\partial_\zeta p|_{wall} = -\frac{1}{\nabla^2\zeta}\left[\rho\,\partial_t\left\{\begin{array}{c}\dot{x}|_{wall}\\ \dot{y}|_{wall}\end{array}\right\}\cdot\nabla\zeta + \partial_\zeta\rho|_{wall}\nabla\xi\cdot\nabla\zeta\right], \qquad (15)$$

where $\dot{x}|_{wall}$ and $\dot{y}|_{wall}$ are the components of the airfoil velocity. Furthermore, by assuming that the grid is orthogonal at the surface, then, $\nabla\xi\cdot\nabla\zeta = 0$. If the airfoil is stationary, the normal pressure gradient vanishes in agreement with boundary-layer theory.

The flow at the wind tunnel sections blocks (2) and (3) is assumed to be inviscid and the Euler equations are solved in these domains. The tunnel walls are assumed to be porous, and two types of porous wall boundary conditions are applied. First, the porous boundary condition is applied according to the formulation presented by Mokry et al.[3] (Chapter 2.0 WALL BOUNDARY CONDITION). Pressure, density, and x-direction velocity, u, are extrapolated from the interior points of the grid. The z-direction velocity, w, is obtained according to Eq. (16)

$$\frac{w}{U_\infty} = \sigma\,\frac{p - p_{plenum}}{\rho_\infty U_\infty^2} \qquad (16)$$

where σ is the porosity parameter of the wall and p_{plenum} is the pressure at the plenum chamber. For $\sigma = 0$, for example, this boundary condition is the same as the flow tangency condition and the wall is treated as being completely solid.

The porous-wall boundary condition can be further modified to account for viscous effects present at this region of the walls as follows. The tangential velocity at the wall is set equal to zero, $u = 0$, and the normal velocity, w, is still obtained according to Eq. (16). In this work, this model is denoted as the porous, viscous boundary condition.

This treatment for the porous-wall boundary condition is quite different from the one adopted in the

previous work.[2] In that study, the porous boundary was modeled by treating some grid cells as solid walls (applying flow tangency) and the others as holes (extrapolating the velocity vector from the interior points). For the previous approach, the grid needed to be approximately uniformly spaced at the porous region. Furthermore, only certain discrete choices in the porosity were allowed. Values of porosity, such as 17%, were very difficult to apply due to the limited number of grid cells along the porous region of the walls. The new model is not dependent on the streamwise grid spacing at the walls and also allows for a continuous variation on the porosity parameter.

Inflow and outflow boundary conditions are imposed on blocks (2) and (3), respectively. For the inflow boundary, flow properties such as pressure, temperature, and velocity are specified while the density is extrapolated from the neighbor interior points. Static pressure is specified for the outflow boundary condition and all other properties are extrapolated from the interior. The other boundaries on the right and on the left of domains (2) and (3), respectively, are updated by linear interpolation from domain (1).

For the parallel version of the code, the exchange of grid boundary data among the three blocks is performed via the Message Passing Interface (MPI) library. The three blocks are solved simultaneously, each one on a node of the PC cluster. The values of the flow variables at the boundaries are then transferred at the end of each iteration.

E. Grid Motion

The problem considered is the numerical prediction of the flow around an oscillating airfoil inside a wind tunnel. This problem requires use of deforming grids and problems arise for the adjustment of the grid which accounts for the motion of the airfoil. The wind tunnel walls are fixed at all times while the airfoil is moving. Therefore, the grid must be deformed every time step in order to adjust to the relative movement between the airfoil and the walls.

The required deformation of the grid is obtained by dividing the whole domain of the C-type grid around the airfoil block (1) into four regions. These regions are distributed along the main block as shown in Fig. 2. The first region is called A_p and corresponds to the portion of the block that is close to the surface of the airfoil and used to capture the viscous flow effects. In this region the mesh does not deform but simply rotates and translates as a solid body, following the same rotation and translation of the airfoil. This means that there is no volumetric change of the grid cells in the region A_p. Another region, denoted C, is the one close to the wind tunnel walls and to the blocks (2) and (3) overlapping sections. This region also remains fixed at all times and, therefore, the grid points do not change in time for an observer sitting on the wind tunnel walls.

The region A_w corresponds to the "wake" following region A_p. It is adjusted to the movement of the airfoil. The adjustment is done using an algebraic grid generator which redistributes the grid points. Linear interpolation for the grid points along a constant ζ line is applied. This procedure takes into account that the displacement of a grid point in the region A_w is proportional to the relative displacement of the corresponding points (same ζ coordinate) in regions A_p and C. Finally, while the relative location of regions A_w and A_p with respect to the tunnel walls changes, region B (where the grid deformation is the largest) is adjusted to provide a smooth grid between regions A and C. This adjustment, again, is done by means of the algebraic grid generator, but now linear interpolation is performed along constant ξ lines.

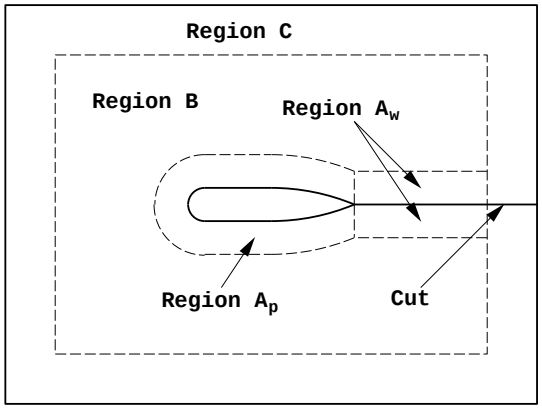

Fig. 2. Schematic of the regions for grid motion.

III. Structural Dynamics

Structural modeling is implemented using a two-degree-of-freedom spring/mass/damper system (Fig. 3) which simulates the bending and twisting of a wing.

A. Governing Equation

The equations governing this motion are:

$$m\ddot{h} - S_\alpha \ddot{\alpha} + D_h \dot{h} + m\omega_h^2 h = L \qquad (17)$$

$$-S_\alpha \ddot{h} + I_\alpha \ddot{\alpha} + D_\alpha \dot{\alpha} + I_\alpha \omega_\alpha^2 (\alpha - \alpha_0) = M \ , \qquad (18)$$

where the dots denote differentiation with respect to time.

Eqs. (17) and (18) are nondimensionalized using reference length c, reference velocity a_∞, reference mass $\rho_\infty \pi (c/2)^2$, and reference inertia $\rho_\infty \pi (c/2)^2 c^2$.

In matrix notation, Eqs. (17) and (18) are:

$$[\mathbf{M}]\{X\}'' + [\mathbf{D}]\{X\}' + [\mathbf{K}]\{X\} = \{F\} \qquad (19)$$

where

$$[\mathbf{M}] = \begin{bmatrix} m & -S_\alpha \\ -S_\alpha & I_\alpha \end{bmatrix}, \; [\mathbf{D}] = \begin{bmatrix} 2\delta_h m\tilde{k}_h & 0 \\ 0 & 2\delta_\alpha I_\alpha \tilde{k}_\alpha \end{bmatrix},$$

$$[\mathbf{K}] = \begin{bmatrix} m\tilde{k}_h^2 & 0 \\ 0 & I_\alpha \tilde{k}_\alpha^2 \end{bmatrix}, \; \{X\} = \begin{Bmatrix} h \\ \alpha - \alpha_0 \end{Bmatrix}$$

and

$$\{F\} = \frac{2}{\pi}\mathbf{M}_\infty^2 \begin{Bmatrix} C_l \\ C_m \end{Bmatrix},$$

where primes are used to denote differentiation with respect to dimensionless time, $\tilde{k}_h = M_\infty k_h$, $\tilde{k}_\alpha = M_\infty k_\alpha$, $\tau = ta_\infty/c$, and the other parameters (i.e., m, I_α,...) are now non-dimensional.

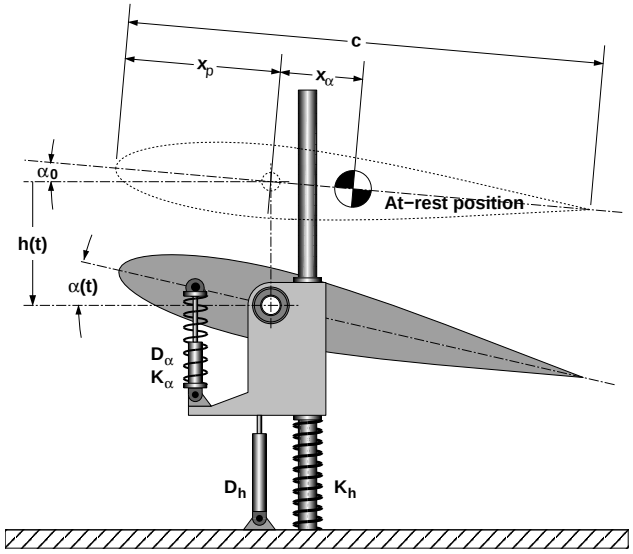

Fig. 3. Schematic of the spring/mass/damper system.

B. Numerical Method

Equation (19) is a system of two, coupled, second-order, ordinary differential equations. Coupling is obtained through the terms containing S_α and the dependence of C_l and C_m on h and α. The system is nonlinear through the nonlinearity of C_l and C_m. Linearization is introduced by treating C_l and C_m as constants, computed from the previous time-step of the flow solution.

Equation (19) is advanced in time by rewriting the system of equations as follows

$$\begin{aligned} \{X\}'' &= [\mathbf{M}]^{-1}\{F\} \\ &\quad - [\mathbf{M}]^{-1}[\mathbf{K}]\{X\} - [\mathbf{M}]^{-1}[\mathbf{D}]\{X\}' \; . \end{aligned} \qquad (20)$$

Rewriting Eq. (20) as a system of two, coupled, first-order equations, one obtains

$$\begin{aligned} \{X\}' &= \{Y\} \\ \{Y\}' &= [\mathbf{M}]^{-1}\{F\} \\ &\quad - [\mathbf{M}]^{-1}[\mathbf{K}]\{X\} - [\mathbf{M}]^{-1}[\mathbf{D}]\{Y\} \; . \end{aligned} \qquad (21)$$

Time integration of the first-order system of Eq. (21) is performed using the 1st-order accurate in time explicit Euler scheme.

As explained in Ref. 1, use of higher order methods to solve the structural dynamics equations does not improve the solution quality because the time steps required for the stability of the thin-layer Navier-Stokes equations yield very high resolution in time for Eq. (21).

IV. Results

One of the most important conclusions of the work performed previously by Castro et al.[2] was the identification of the significance of the porosity of the wind tunnel walls on the prediction of transonic steady and unsteady flow characteristics of the airfoil inside the wind tunnel. The current work was carried out in order to further investigate the effect of porosity of the walls and improve the method of prescribing such a boundary condition. Therefore, the approach adopted was based on the determination of a porous boundary condition that yielded a steady-state surface pressure distribution for the NLR7301 airfoil, in the presence of the wind tunnel walls, which was in best agreement with the experiment performed by Knipfer et al.[9] Once a satisfactory porous boundary condition was determined, the flutter computations were performed. Adjustment of other flow parameters of the experiment, such as inflow and outflow boundary conditions, was not attempted. The wind tunnel test was performed at a Mach number of $M_\infty = 0.768$, an angle of attack of $\alpha = 1.28$ degrees, and a Reynolds number of $Re = 1.727 \times 10^6$. The same flow conditions were used in the present simulation, since no corrections were applied to the experimental data.[9] The plenum pressure was always kept equal to the free-stream pressure ($p_{plenum} = p_\infty$). The results for the steady calculations were used as the start for the unsteady simulations.

All steady-state and unsteady computations were performed using a C-type 281 × 81 point main block grid (1), shown in Fig. 4, which was generated from the original NLR7301 airfoil surface data. Blocks (2) and (3) were Cartesian-type and contained 41 × 41

and 41 × 61 points along the streamwise and normal directions, respectively. The Spalart-Allmaras (SA) turbulence model was used throughout the course of this work.

All the computations were performed in a time-accurate mode using a constant time step. For fixed angles of incidence, the solution was run for a long time after convergence in residuals so that variations in all aerodynamic coefficients were reduced to machine zero. This was done in order to ensure that all flow disturbances from the initial transients were swept out of the domain. At convergence, all solutions at fixed angles of incidence did not exhibit any unsteadiness.

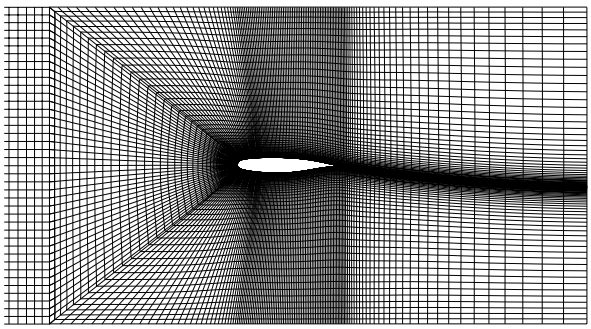

Fig. 4. C-type grid in the vicinity of the NLR7301 airfoil.

A. Grid Deformation Capability

To validate the handling of the deforming grid, a test was performed where the boundary of region B in block (1) remained fixed, but the interior points of B performed sinusoidal oscillations. Grid points in blocks (2) and (3) as well as the ones in regions A_p, A_w, and C of block (1) remained fixed. The reduced frequency of the oscillation of grid points in region B was set to $k = 0.3$ and the maximum amplitude to $\Delta h = 0.05$.

This test is initialized from a steady-state solution for a solid wind tunnel wall boundary condition at a non-dimensional time of $\tau = 46.72$. Ideally, the solution should remain constant after the oscillation of the grid points in region B had started. Nonetheless, because of numerical errors and movement of grid points across a shock wave, some variation of the aerodynamic coefficients should be expected. The results for the test are shown in Fig. 5. The amplitudes of the deviation of the aerodynamic coefficients are $\Delta c_L = 3.2 \times 10^{-4}$, $\Delta c_D = 1.6 \times 10^{-5}$, and $\Delta c_m = 6.4 \times 10^{-5}$. The results of a DFT analysis on the deviations is presented in Fig. 6. One can see that the non-dimensional frequency of the signal is computed as $\hat{f} = 0.0375$. This corresponds to a reduced frequency of $k = 0.307$ which is approximately the reduced frequency in which the grid was oscillating. These small-amplitude oscillations are considered to be acceptable.

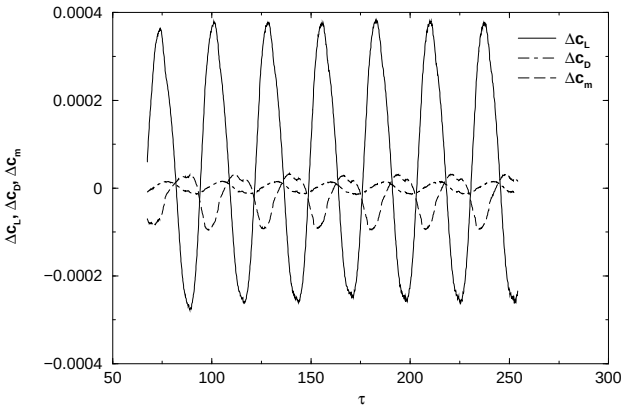

Fig. 5. Deviation of the aerodynamic coefficients for an oscillating grid.

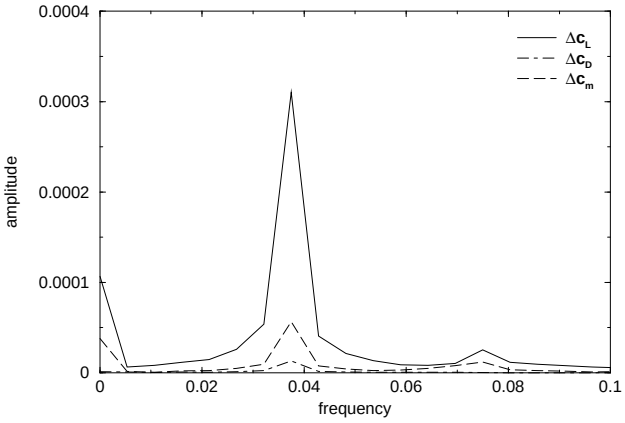

Fig. 6. DFT analysis of the deviation.

B. Steady-State Computations

Another task performed in the present work was the evaluation of the ability of the parallel version of the solver to reduce the computational time required for convergence of a particular problem. A simulation for a solid wind tunnel wall was run and a reduction of approximately 10% in the time required to achieve 5,000 iterations was found. Note that the three-block grid used in this case was not favorable for a substantial reduction in the computational time, since the size of the first block corresponded to approximately 85% of the total number of grid cells and thin layer Navier-Stokes equations were solved in it while Euler equations were solved in the other two blocks. Consequently, a 10% reduction in the computational time was quite satisfactory for this particular case and demonstrated the feasibility of the parallel version of the code. The pressure distribution obtained with the parallel code for a solid-wall case is shown in Fig. 7. An unsteady case was also run in order to check the

parallel version of the code and it yielded the same results as the single processor solution.

The model for the porosity of the wall, based on the theory presented by Mokry et al.,[3] Eq. (16), was evaluated next. The pressure distributions for 25% and 50% wall porosity parameters are presented in Fig. 8. The porous, inviscid boundary condition was used for these cases. It can be seen that a better agreement with the experiment is achieved for a porous boundary condition than for the solid wall.

The porous, viscous model was also tested for porosity parameters of $\sigma = 0.25$ and $\sigma = 0.50$ and yielded slightly better agreement with the experiment than the porous, inviscid model. The comparison of the pressure distributions with the experimental results for this case are shown in Fig. 9. The porosity parameter of $\sigma = 0.25$ seems to yield a better agreement with the time-averaged pressure distribution of Ref. 9, predicting a better location for the upper shock.

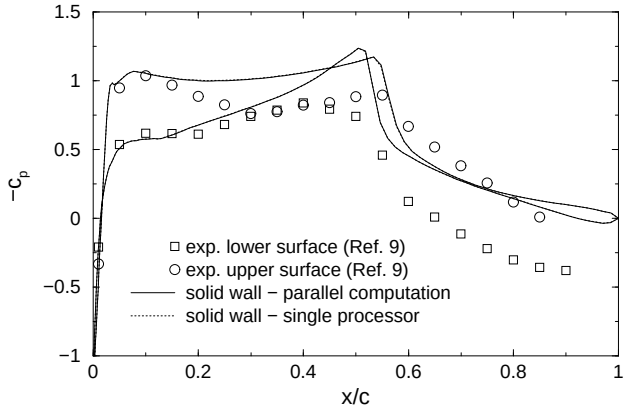

Fig. 7. Comparison of surface pressure coefficient for solid walls.

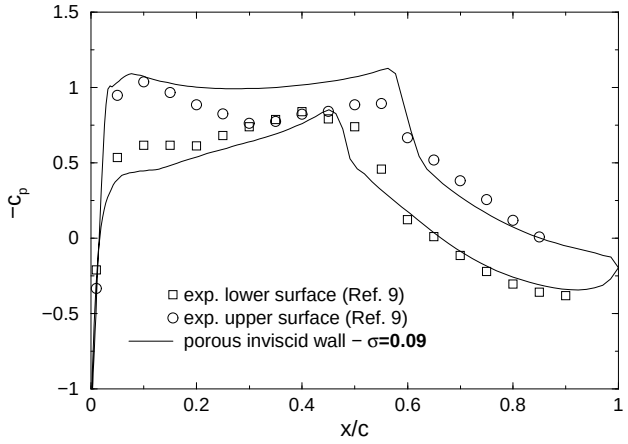

Fig. 8. Surface pressure distribution for a porous, inviscid boundary condition at the tunnel walls.

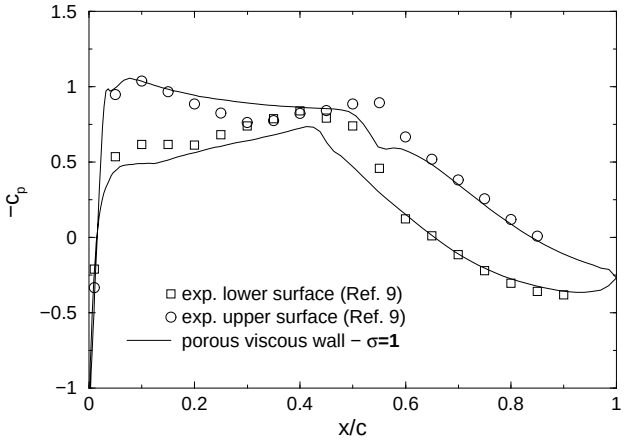

Fig. 9. Surface pressure distribution for a porous, viscous boundary condition at the tunnel walls.

In summary, the steady-state computations demonstrate that the porosity of the walls has a very strong influence on the computed flow field around the NLR7301 airfoil. Additionally, the method of applying the corresponding boundary condition is influential.

C. Flutter Computations

Based on the conclusions drawn from the steady computations, the flutter simulations were performed using the porous model for the wind tunnel walls. The nominal conditions of the wind-tunnel test were preserved, namely $M_\infty = 0.768$, $\alpha_i = 1.28$ degrees, and $Re = 1.727 \times 10^6$, as well as the spring-neutral angle of attack $\alpha_0 = 1.91$ degrees. Note that these values were modified in Ref. 1, to account for wind-tunnel interference, to $M_\infty = 0.753$, $\alpha_{ic} = -0.08$ degrees, $Re = 1.727 \times 10^6$, and $\alpha_{0c} = 0.635$ degrees. All time-accurate flutter computations were performed assuming fully turbulent flow using the Spalart-Allmaras turbulence model. The computations predicted flutter in two-degree-of-freedom. Limit-cycle oscillations (LCO) were computed in agreement with the wind tunnel test.

In the experimental test case,[9] limit-cycle oscillations in pitch and plunge were reported. The experiment was conducted at a total pressure of 0.45 bar and a dynamic pressure of 0.126 bar. A time-averaged angle of attack of $\bar{\alpha} = 1.28$ degrees was measured for an angle of attack at wind-off condition of $\alpha_0 = 1.91$ degrees which is equivalent to the spring-neutral angle of attack in the numerical simulation. The porosity parameter associated with the perforated wall of the DLR-Göttingen wind tunnel was stated as $\sigma = 0.25$. The holes in the wall were drilled with an angle of 30 degrees with respect to the surface of the wall. No measurements of the pressure at the wall were performed, therefore, the plenum pressure was assumed to

be the free-stream pressure in the present study. The dimensionless structural parameters of the experiment are summarized in Table 1. The same parameters were used for the aeroelastic computation.

Table 1: Structural parameters

$x_p =$	0.2500	$k_\alpha =$	0.3330
$x_\alpha =$	0.0484	$k_h =$	0.2540
$m =$	946.00	$\delta_\alpha =$	0.0041
$I_\alpha =$	33.900	$\delta_h =$	0.0073

Initially, the flutter computations were started based on a porosity parameter of $\sigma = 0.25$. Time history of the angle of attack for a porous, inviscid boundary condition at the tunnel walls is shown in Fig. 10. Note that LCO has not been achieved. The initial oscillations damp out and the computations converge to steady value of the angle of attack. Next, a porous, viscous boundary condition was evaluated. Time history of the angle of attack for this case is presented in Fig. 11. For a porous, viscous model, LCO is clearly achieved but the amplitude is higher than the reported experimental values of Knipfer et al.[9] The flutter results for the computations are summarized in Table 2.

Table 2: Flutter results

method	$\bar{\alpha}$ [deg]	$\hat{\alpha}$ [deg]	$\hat{h}$ [mm]	f [Hz]	Φ [deg]
Exp.$_a$	1.28	0.18	0.65	32.85	176.7
SA$_b$	1.19	0.00	0.00	34.4	166
SA$_c$	1.15	1.70	4.68	34.5	165
SA$_d$	1.24	0.78	2.9	36.7	149
SA$_e$	0.07	3.78	11.1	32.30	171.8

$_a$ = without wind tunnel corrections.
$_b$ = with porous, inviscid wall; $\sigma = 0.25$.
$_c$ = with porous, viscous wall; $\sigma = 0.25$.
$_d$ = previous work; with 50% porosity.
$_e$ = Ref. 1; fully turbulent (unbounded computation).

Table 3: LCO computations

σ	$\bar{\alpha}$ [deg]	$\hat{\alpha}$ [deg]	$\hat{h}$ [mm]	f [Hz]	Φ [deg]
0.12	1.10	0.01	0.04	34.7	164
0.16	1.11	0.38	1.09	34.5	165
0.20	1.12	1.51	4.25	34.6	165
0.25	1.15	1.70	4.68	34.5	165
0.30	1.17	1.69	4.61	34.3	167
0.50	1.17	1.20	3.19	34.5	166

The computations for $\sigma = 0.25$ show that the type of boundary condition for the porous wall can lead to different unsteady solutions. LCO is obtained for the porous, viscous boundary condition in which the flow is essentially vertical at the wall, but for the porous, inviscid boundary condition, the flow is almost tangent to the wall and the motion is damped. In fact, neither the viscous nor the inviscid boundary condition accurately models the details of the near-wall flow of the experiment. The experiment used holes drilled at 30 degrees imposing a curvature to the flow. The approach adopted in the present work uses two extreme conditions of flow curvature represented by the porous, inviscid and viscous boundary conditions (tangent and normal, respectively). The curvature of the flow in the experiment is in between these two extreme values. Fortunately, the experimental LCO amplitudes also lie in between the computed ones for the two types of boundary condition. This suggests that the porous boundary condition for the wind-tunnel walls significantly improves the computations of LCO for the NLR7301 inside the DLR-Göttingen wind tunnel.

In order to study the influence of the porosity parameter of the wind-tunnel walls in the prediction of limit-cycle oscillations, a parametric variation of σ was conducted. First, a porous, inviscid boundary condition was used to compute a solution for a porosity parameter of 50%. The time history of the angle of attack shows that the LCO was never achieved and the initial oscillations damp out as illustrated in Fig. 12. Next, several cases were run for different values of the porosity parameter using the porous, viscous boundary condition. The LCO amplitudes obtained in those runs are shown in Fig. 13. These results are also provided in Table 3. It is clear that the porosity parameter also has a significant influence on the LCO amplitudes. Because of the flow curvature at the porous walls, the LCO amplitudes are expected to be smaller than the ones presented in Fig. 13 and Table 3. Nevertheless, the influence of the porosity parameter is believed to be the same. Final results for the flutter computations, including flutter frequency, phase, amplitudes $\hat{\alpha}$ and $\hat{h}$, and mean angle of attack $\bar{\alpha}$, are shown in Tables 2 and 3.

The influence of the tunnel blockage was also investigated. Three more cases were run with different heights of the wind-tunnel test section, H. The nominal condition for the experiment was $H = 1.0m$ which yields $H/c = 3.33$. The additional cases represented $H/c = 5.00$, $H/c = 6.67$, and $H/c = \infty$ (unbounded flow). All nominal values of the experiment were preserved. Note that the unbounded solution, in this case, is different from the results obtained in Ref. 1, due to the corrected free-stream conditions they used. The

history of the angle-of-attack amplitude for these cases can be seen in Fig. 14. The porous, viscous boundary condition with $\sigma = 0.25$ was used at the tunnel walls in all the cases but the unbounded flow. The results show a tendency of decreasing the LCO amplitudes as the height of the test section H is increased. For $H/c = 5.00$, the oscillations are already damped out as in the unbounded flow solution. As expected, the results tend to the unbounded flow solution as H/c is increased. These results also show that, depending on the value of H/c chosen for the wind-tunnel test, the flutter characteristics of the measurements may differ significantly from the free-flight situation.

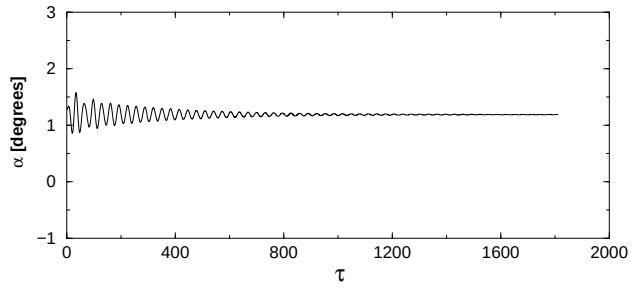

Fig. 10. Angle of attack history for $\sigma = 0.25$ and porous, inviscid boundary condition.

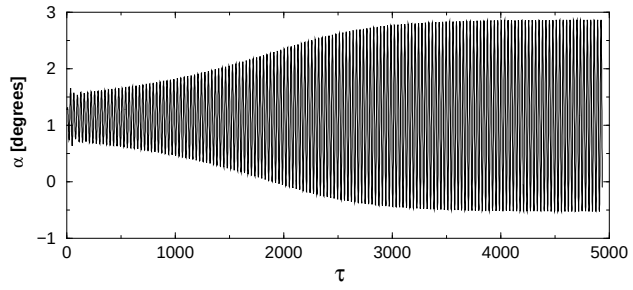

Fig. 11. Angle of attack history for $\sigma = 0.25$ and porous, viscous boundary condition.

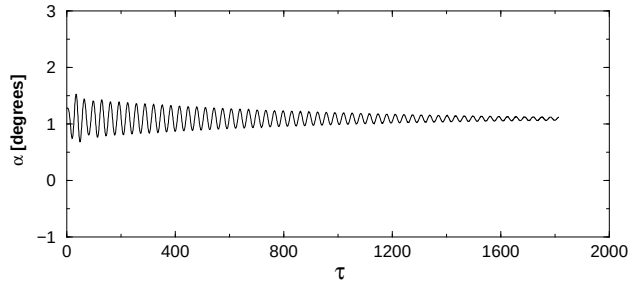

Fig. 12. Angle of attack history for $\sigma = 0.50$ and porous, inviscid boundary condition.

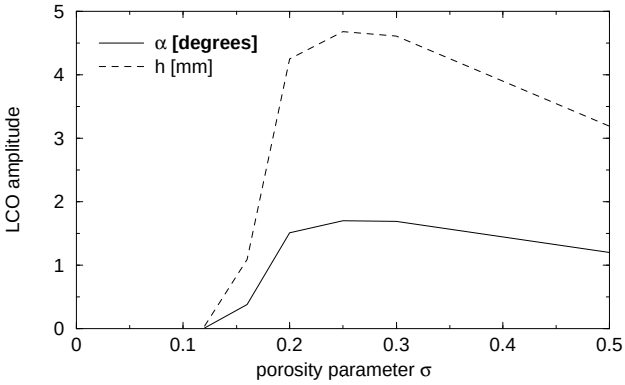

Fig. 13. Variation of LCO amplitudes with the porosity parameter.

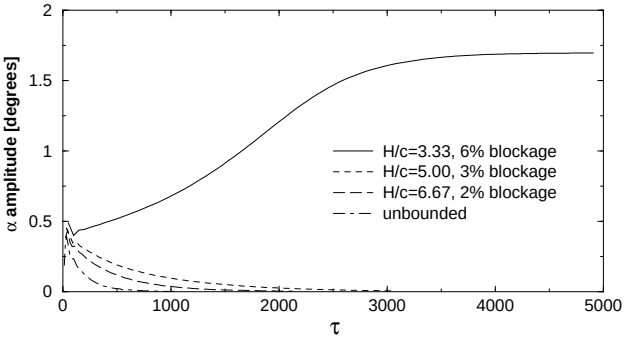

Fig. 14. Variation of LCO amplitudes with the solid blockage.

The influence of the Mach number on the flutter characteristics of the NLR7301 airfoil including tunnel walls was studied as well. In order to save computational efforts, the porous, inviscid wall boundary condition was used. This type of wall boundary condition requires a much shorter computational time to achieve LCO. The time history of the angle of attack amplitudes for some Mach numbers is presented in Fig. 15 for both tunnel and unbounded solutions. The amplitudes for the wind tunnel solutions were always higher than the ones for unbounded flow in the Mach number range of the computations.

The results obtained in this work show that the porosity parameter, the solid blockage of the test section, and the Mach number all have a strong influence on the prediction of the transonic flutter characteristics of the NLR7301 airfoil, as indicated in Figs. 10 through 15. The type of boundary condition used for the porous wind tunnel wall is also influential. The computed amplitudes of $\hat{\alpha}$ and $\hat{h}$ are larger than the ones measured in the experiment[9] for a porous, viscous boundary condition but lower for a porous, inviscid one. The type of boundary condition has only a small effect on the prediction of flutter frequency and inter-modal phase angle. These values were pre-

dicted more closely in the present work than in Ref. 2. Therefore, it is considered that an improvement was obtained with respect to the previous work.[2] The predicted flutter frequency deviates from the experimental value by 4.9% and the inter-modal phase angle by 11 degrees. Nonetheless, these parameters were predicted more closely by the unbounded flow computations of Weber et al.[1] The values of frequencies, amplitudes, and phase angles were calculated by means of a DFT-analysis of the last 10 cycles.

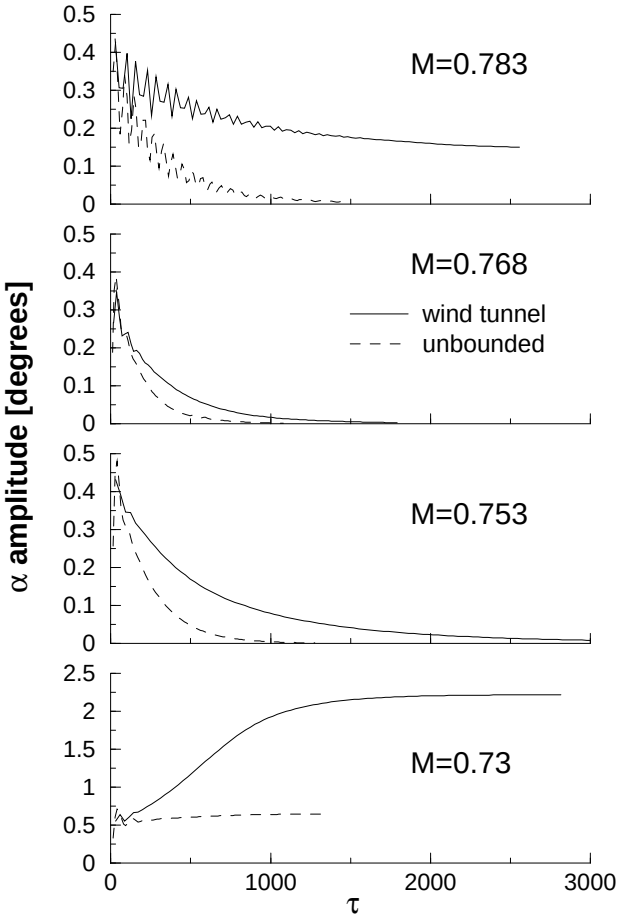

Fig. 15. Variation of angle-of-attack amplitudes with Mach number.

Although the amplitudes were overpredicted or underpredicted depending on the type of wall boundary condition, the limit-cycle oscillation phenomenon was correctly predicted and the frequency and the inter-modal phase angle were computed within a reasonable accuracy. It must be kept in mind that the plenum chamber pressure was assumed to be the free-stream pressure. Also, it is inevitable that additional uncertainty factors exist. It appears, then, that the wind tunnel porosity model used in the present computations yields a significant improvement on the prediction of flutter characteristics of wind tunnel flows.

V. Conclusions

A parallel version of the solver was implemented and compared with the single processor version. The parallel code reduced the wall-clock time required for a solution and yielded identical results to the single processor solution for both steady-state and unsteady computations.

An improved method of modeling the porosity of the wind tunnel walls was implemented. Two different models were tested. One adopted the approach presented by Mokry et al.,[3] in which the normal velocity through the porous region was proportional to the pressure difference between the plenum chamber and the test section. The other consisted of a viscous approach assuming the same normal velocity but no tangential component at the porous region of the wind tunnel walls. The modeling of the tunnel wall porosity and the way the corresponding boundary condition was applied (viscous or inviscid) were both found to significantly affect the numerical predictions of the steady-state and flutter characteristics. The improved porosity models also allowed more flexibility for the generation of the grid because the requirement for an almost equally spaced grid at the porous region of the walls was no longer necessary.

The transonic two-degree-of-freedom bending/torsion flutter analysis of the NLR7301 supercritical airfoil section with tunnel walls modeled using the improved porosity boundary condition showed a significant influence of the porosity parameter on the prediction of the limit-cycle amplitudes. On the other hand, the computed phase angle between pitch and plunge motions and the flutter frequency were not significantly affected by the porosity parameter.

The main conclusion of the present work is that the limit-cycle flutter amplitudes can be quite sensitive to the chosen wind tunnel wall porosity. In fact, flutter may be suppressed completely for a sufficiently small porosity. Furthermore, the free-flight flutter behavior may differ substantially from the behavior found in a porous wind tunnel depending on the chosen porosity and blockage ratio. Consequently, further investigation is necessary to assess the modeling of the porous wall boundary condition and the correlation between wind tunnel tests and free-flight conditions.

References

[1]Weber, S., Jones, K. D., Ekaterinaris, J. A., and Platzer, M. F., "Transonic Flutter Computations for a 2-D Supercritical Wing," AIAA Paper 99-0798, 1999.

[2]Castro, B. M., Ekaterinaris, J. A., and Platzer, M. F., "Transonic Flutter Computations for the NLR 7301 Airfoil Inside a Wind Tunnel," AIAA Paper 2000-0984, 2000.

[3]Mokry, M., Chan, Y. Y., and Jones, D. J., "Two-Dimensional Wind Tunnel Wall Interference," AGAR-Dograph No. 281.

[4]Sanz, W. and Platzer, M.F., "On the Navier-Stokes Calculation of Separation Bubbles With a New Transition Model," *Transaction of the ASME*, Vol. 120, 1998, pp 36-42.

[5]Ekaterinaris, J. A. and Menter, F. R., "Computation of Oscillating Airfoil Flows with One- and Two-Equation Turbulence Models," *AIAA Journal*, Vol. 32, No. 12, 1994, pp. 2359-2365.

[6]Ekaterinaris, J. A., Sorensen, N. N., and Rasmussen, F., "Numerical Investigation of Airfoil Dynamic Stall in Simultaneous Harmonic Oscillatory and Translatory Motion," *ASME Journal of Solar Energy Engineering*, Vol. 120, 1998, pp 75-83.

[7]Ekaterinaris, J. A., Cricelli, A. S., and Platzer, M. F., "A Zonal Method for Unsteady, Viscous, Compressible Airfoil Flows," *Journal of Fluids and Structures*, Vol. 8, 1994, pp. 107-123.

[8]Jones, K. D. and Platzer, M. F., "Airfoil Geometry and Flow Compressibility Effects on Wing and Blade Flutter," AIAA 98-0517, 1998.

[9]Knipfer, A., Schewe, G., and Wendt, V., "Numerische und experimentelle Untersuchungen an einem schwingenden NLR7301-Profil in transsonischer Stroemung, Teil 1: Flattern und erzwungene Schwingungen," DLR Bericht IB 232-98 J 05, 1998.

[10]Schewe, G., and Deyhle, H., "Experiments on Transonic Flutter of a Two-Dimensional Supercritical Wing with Emphasis on the Non-Linear Effect," Proceedings of the Royal Aeronautical Society Conference on Unsteady Aerodynamics, London, 1996.

[11]Thomas, P. D. and Lombard, C. K., "Geometric Conservation Law and its Applications to Flow Computations on Moving Grids," *AIAA Journal*, Vol. 17, No. 10, 1979, pp. 1030-1037.

[12]Osher, S. and Chakravarthy, S. R., "A New Class of High Accuracy TVD Schemes for Hyperbolic Conservation Laws," AIAA Paper 85-0363, 1985.

[13]Chakravarthy, S. R. and Osher, S., "Numerical Experiments with the Osher Upwind Scheme for the Euler Equations," *AIAA Journal*, Vol. 21, No. 11, 1983, pp. 1241-1248.

[14]Steger, J. L. and Warming, R. F., "Flux Vector Splitting of the Inviscid Gas Dynamic Equations with Applications to Finite-Difference Methods," *Journal of Computational Physics*, Vol. 40, 1981, pp. 263-293.

[15]Baldwin, B. S. and Lomax, H., "Thin Layer Approximation and Algebraic Model for Separated Turbulent Flow," AIAA Paper 78-257, 1978.

[16]Baldwin, B. S. and Barth, T. J., "A One-Equation Turbulence Transport Model for High Reynolds Number Wall-Bounded Flows," NASA TM 102847, 1990.

[17]Spalart, P. R. and Allmaras, S. R., "A One-Equation Turbulence Model for Aerodynamic Flows," AIAA Paper 92-0439, 1992.